Optimization of hydration conditions of low calcium cements

Maria Inês Bayão Horta Mesquita da Cunha

ABSTRACT

This work intended to study the hydration mechanisms and optimization of hydration conditions in newly developed amorphous hydraulic binders with a Ca/Si ratio of 1.1. Two different cooling procedures were used in the production of these amorphous binders: air-cooling; and water-cooling. Pastes were produced from these samples and the hydration evolution in its early age was followed by means of XRD, SEM-EDS, FTIR-ATR, TGA, isothermal calorimetry and compressive testing. The assessment of the hydration mechanisms involved in these particular systems indicated that theses amorphous binders hydrate by rearranging their $Q^0, Q^1 \text{ and } Q^3$ units and forming structures consisting of hydrated Q^2 units of tobermorite and amorphous $C\text{-}S\text{-}H$. The study of the optimization of hydration conditions focused on the evaluation of two important parameters, namely the granulometry and the water/cement ratio. Two sets of samples were analysed by means of the techniques previously mentioned as well as by viscosity testing. For the study on the optimization of hydration conditions, six different samples where produced on which the W/C ratio was changed, at first, and then the granulometric distribution. The study of the optimization of hydration conditions study allowed to determine which pair of W/C ratio/granulometric distribution would result in better performance either in workability or in mechanical strength.

1. INTRODUCTION

According to the global cement database the production of cement has been increasing over the years having increased over 3.6% between 1990 and 2014 [1]. This trend is expected to continue, making the sustainability of this material a very important issue in modern society. Portland cement is the most used type of cement but its production is associated with the release of 842kg of CO_2 per ton of clinker produced [2] making the reduction of this emissions an important and difficult challenge mainly because of the need to align the social-economic development and the international objectives for the reduction of greenhouse gases.

Most of the CO_2 produced in the Portland cement's production comes from the decarbonation of limestone (~55%) with the excess of the emissions attributed to fuel burning, mining and transportation. The reactivity of Portland cement is based on the reactivity of four phases: alite (C_3S), belite (C_2S), tricalcium aluminate (C_3A) and tetracalcium aluminoferrite (C_4AF). The need for calcium incorporation affects directly the capacity to reduce CO_2 emissions. Indeed, reducing calcium incorporation leads to progressively less reactive calcium silicate phases.

In a recent publication from the same project in which this research is inserted [3], a decrease in C/S ratio with a full amorphization of the material was proposed. This approach revealed itself successful both in decreasing CO_2 emissions and in producing a hydraulic binder. The present work is a continuation of that project with three main objectives: determine the best cooling method for the molten material; determine the hydration mechanisms of this amorphous hydraulic binder; and optimize the hydration conditions of this binder.

2. EXPERIMENTAL PROCEDURE

2.1. Materials and processing conditions

The amorphous hydraulic binder used in this work was produced using a combination of common raw materials in the cement industry. Table 1 presents the composition of each raw material used to make the binder with an overall C/S molar ratio of 1.1. After mixing the raw materials, 250g of that mixture was pressed to a disc shape with 10cm

diameter and approximately 3cm height with a force of around 100kN. The resulting disc was then broken into three pieces to fit the platinum crucible in which it was placed in the electric furnace.
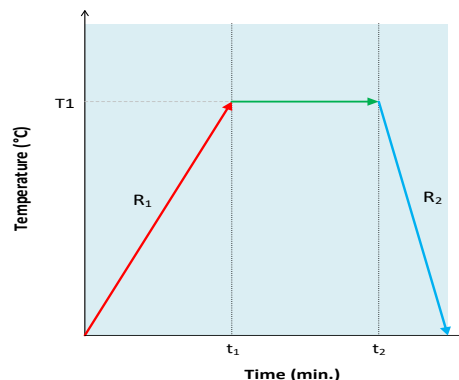

Figure 1 - Production procedure of the amorphous hydraulic binders.

The production process used is schematically exemplified in Figure 1 and consisted on the following steps: a) heating the material at a rate of 25ºC/min until T_1=1550ºC; b) maintaining T_1 for 60 minutes to ensure total mixture fusion and homogenization; c) cooling. The last stage of cooling was done by one of two ways: air cooling at room temperature by pouring the melt onto a stainless-steel plate; water cooling by pouring the melt into a tank of water at ambient temperature.

After water cooling, the amorphous material obtained was placed in an oven at 105ºC to dry for approximately 30 minutes to ensure the removal of all free water. When doing the air cooling technique this stage is not necessary. The dried amorphous material was then ground in a ring mill with propanol, followed by a drying step in a stove at 50ºC for 30 minutes. The grinding time varies with the intended particle size and this was one of the variables in the optimization study along with the water/binder weight ratio used to produce the pastes. Three grinding times were tested leading to three particle sizes: 180s, 120s and 45s. The water/binder weight ratio used in the optimization study were 0.325, 0.375 or 0.425. In the hydration mechanism study both the grinding time and the water/binder used were kept constant: 180s and 0.375. In the hydration mechanisms study the pastes were poured into plastic bags with approximately 10g each that were then vacuum

sealed, whereas in the optimization study they were poured into moulds with 20x20x40 mm³. All the samples were cured in a moisture-controlled environment with a relative humidity of 95% and a temperature of 20ºC. After four days of hydration all the prims where demoulded and left to hydrate in the same storage place until the time they were tested.

2.2. Characterization methods

Anhydrous and hydrated samples where tested to characterize the material both before and after hydration to assess mechanical performance and phase development.

In the hydration mechanisms study, characterization was made by TGA, FTIR-ATR, XRD and Rietveld analysis, isothermal calorimetry and SEM imaging. In the optimization study, samples were characterized by the same named techniques and also by compressive testing and by viscosity measurements.

All samples had their hydration monitored by isothermal calorimetry using a TAM air equipment.

Compressive testing was performed in the 20x20x40 mm³ paste prisms after 4, 7, 14 and 28 days of hydration. These tests were performed in an Ibertest Autotest 400/10 equipment at a force rate of 2.4kN/s. After compression testing the samples were ground in an agate mortar and dried for half an hour at 105ºC, after which they were sealed in vacuum for further characterization. The exception was for the TGA, that was made immediately after the compression testing. The samples that were produced in bags rather than in prims did not undergo compressive testing.

Thermogravimetric analysis (TGA) was made to assess the percentage of structural water retained in the structure after hydration. This was made in a ELTRA equipment with constant heating rates between stages in which the temperature was kept constant until the mass stabilized. In the first stage from room temperature until 105ºC the heating rate applied was 4ºC/min, in the second stage from 105ºC until 250ºC the heating rate was 10ºC/min, while in the last two stages between 250ºC and 500ºC and between 500ºC and 900º, the heating rate was 15ºC/min. All the unbound water was considered to be lost until 105ºC while the mass lost between 105ºC and 500ºC would account for the loss of all structural water in the sample.

FTIR-ATR spectroscopy was performed both in anhydrous powders and in dried pastes. The anhydrous powders were used neat and the dried pastes were ground by hand. The FTIR spectra was obtained with a Bruker Alpha Platinum-ATR spectrometer. The spectra were collected in the medium IR range from 400 to 4000cm⁻¹, with a 4cm⁻¹ resolution and 24 accumulations.

X-ray diffraction was performed in powder samples with a PANalytical X'Pert Pro diffractometer using a monochromatic CuKα1 radiation of $\lambda = 1.54059\,\text{Å}$, in a θ/2θ configuration. Data from the samples was collected between 5 to 70° (2θ) with a X'Celerator RTMS (Real-Time Multiple Strip) detector while the sample rotated at 16rpm to enhance particle statics. A fixed divergence slip of 1/2º, a fixed anti-scatter slit for the incident beam of 1º and a fixed anti-scatter slit for the diffracted beam of 1/2º were used. The X-ray tube worked at 45kV and 40mA. For the quantification of the amorphous content in the samples, 20% in weight of aluminium oxide (99.9% α-Al₂O₃ da Alfa Aesar) was added to each one. Phase quantification was then performed by Rietveld analysis using PANalytical HighScore Plus software. For the Rietveld fitting the following phases were used: wollastonite with the reference code ICDD 96-900-5778; Pseudowollastonite with the reference code ICDD 96-900-2180; Tobermorite 9Å with the reference code ICSD 87689; and aluminium oxide with the reference code ICDD 96-100-0060 all from the COD database.

SEM imaging was conducted in freshly fractured surfaces and was performed by a FEG-SEM JEOL 7001F equipment working at a voltage of 15kV. For the EDS mapping the samples were cut, polished and mounted in epoxy resin prior to the mapping. This allowed for a better mapping capacity due to a less rough surface. The EDS detector coupled to the SEM equipment was an Oxford 250.

For the samples in the optimization study, viscosity testing was also performed in order to help workability evaluation of each sample. This test was performed in a Brookfield engineering labs viscometer LV model, producing 100g of paste for each sample.

Table 1 – Raw materials composition and its combination used to produce the amorphous hydraulic binders of C/S=1.1.

Raw Materials	Composition (wt. %)									
	Wt. %	Lost on ignition	SiO₂	Al2O₃	Fe₂O₃	CaO	MgO	SO₃	K₂O	Na₂O
Fly-Ash	2.28	4.54	54.48	22.82	8.29	3.78	1.49	0.11	1.76	0.59
Sand	33.58	0.37	96.94	1.29	0.16	0.00	0.02	0.00	0.52	0.11
Slag	2.11	0.00	13.90	8.26	43.54	21.18	6.06	0.40	0.00	0.00
Limestone	62.02	43.9	0.11	0.09	0.08	55.6	0.17	0.02	0.01	0.02
$C/S = 1.1$	100	--	33.97	1.01	0.29	34.57	0.15	0.01	0.22	0.06

3. RESULTS AND DISCUSSION

3.1. Hydration mechanisms

In this study two types of samples were tested: samples that underwent air cooling after exiting the oven (Sample A), and the ones that were water cooled (Sample B). Both types were ground for 180s and were hydrated with a W/C ratio of 0.375.

3.1.1. Isothermal Calorimetry

Samples A and B both showed heat flow curves similar to that of alite's hydration [4], [5]. Even though they share similar shapes, both the heat released by the samples and the hydration time at which the peak of hydration occurs are very different within each other and when compared to alite's hydration curve. Alite's hydration peak occurs

approximately at 9 hours of hydration and has a maximum heat release at that point of 4mW/g. Samples A and B on the other hand have their peaks at 48 and 16 hours, respectively, and maximum heat releases of 70 and 180µW/g.

3.1.2. XRD/Rietveld

The X-ray diffractograms of sample A and B showed that both are almost fully amorphous. In Table 2 and Table 3 the results from Rietveld analysis of the samples A and B at all hydration times are shown. Sample A presents a lower amount of amorphous content than sample B due to the lower cooling rate associated with the production of sample A, resulting in the formation of higher amounts of crystalline phases. Upon hydration, no Portlandite is formed in neither sample. However, there is evidence of the presence of an increasingly higher content of semi-crystalline tobermorite-like structures (C-S-H), falling in agreement with the reported by Santos *et al.*[3]. Nevertheless, in their study Santos *et al.*[3] reported evidence of the presence of tobermorite 11Å while in the present study tobermorite formed is a less hydrated one, tobermorite 9Å.

As hydration proceeds, there is an apparent consumption of wollastonite and pseudowollastonite crystalline phases occurring in both samples A and B. This might be a result of the carbonation of the wollastonite type phases [6], [7]. There is also a slight increase in the amount of tobermorite 9Å as hydration proceeds but, however, still within the error

associated with the technique [8]. Besides the error associated with the technique there is also a problem concerning the identification of this phase: the area where its main peaks are located is the same where the ones from wollastonite are located. Notwithstanding this it must be pointed out that all the variations are in the same direction. Despite all the problematic associated with the quantification of the phases, there is a good fit between the calculated and the experimental curves.
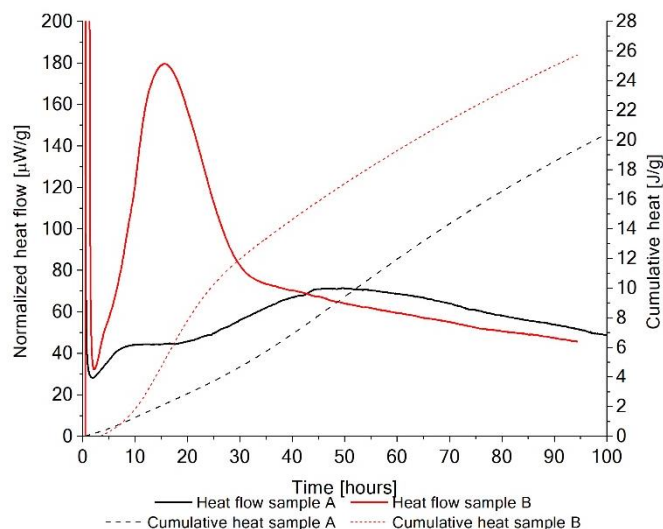
Figure 2 – Heat flow and cumulative heat curves for both types of samples. Curves in red correspond to Sample A and curves in black to Sample B

Table 2 – Rietveld analysis of Sample A at different hydration times.

Age (hours)	Phases (wt.%)			
	Amorphous	Wollastonite	Pseudowollastonite	Tobermorite 9Å
Anhydrous	90.3	2.7	7.0	-
1	89.7	3.0	7.3	0.1
5	91.3	2.4	6.0	0.3
8	89.5	2.9	7.6	0.0
13	89.9	2.9	7.1	0.2
17	92.3	2.1	5.4	0.2
21	89.2	2.9	7.5	0.5
30	90.9	2.4	6.2	0.4
40	90.9	2.4	6.4	0.3
44	89.9	2.7	6.7	0.6
49	89.7	2.4	6.4	1.5
53	90.4	2.3	6.0	1.3
68	91.2	2.1	5.5	1.2
76	91.0	2.2	6.2	0.6
87	91.1	2.0	5.4	1.5
96	92.3	2.1	5.2	0.4

Table 3 - Rietveld analysis of Sample B at different hydration times.

Age (hours)	Phases (wt.%)		
	Amorphous	Wollastonite	Tobermorite 9Å
Anhydrous	98.7	1.3	-
1	97.7	1.2	1.1
5	97.9	1.2	0.9
9	97.7	1.1	1.2
13	98.4	0.9	0.7
17	98.4	0.7	1.0
21	98.0	1.0	1.0
31	98.6	0.8	0.6
86	98.2	0.9	0.9

3.1.3. FTIR-ATR

Figure 3 shows the FTIR spectrum of the anhydrous Samples A and B. These spectra are dominated by four main regions between 400-600cm⁻¹, 600-775cm⁻¹ and 780-1200cm⁻¹. In the region between 780-1200cm⁻¹ three distinct bands are shown *(i), (ii)* and *(iii)*, and are dominated by the stretching modes of the non-bridging oxygens in the Si-O bond for Q¹ (900cm⁻¹) and Q² (950cm⁻¹) units [9]–[13]. The bands *(i)* and *(ii)* are more intense in sample A and have been associated to the stretching of the non-bridging oxygen bonds of Si-O in Wollastonite structures [12]. The fact that band *(ii)* is

wider is due to the additional contribution at this wave number of the stretching modes of the Si-O bond in Q² units. Band *(iii)* has been associated with the stretching vibrations of the Si-O in Q⁰ and Q¹ units. In the region between 600-775cm⁻¹ two bands were identified: one band *(iv)* that is more evident in sample A and that has been attributed to the stretching modes of Si-O-Si in three-membered ring structures [10], [12]; and band (v) attributed to Si-O-Si bond vibrations in SiO4 tetrahedra [14]. Finally, in the region between 400-600cm⁻¹ the band (vi) is assigned to the asymmetric bending of Si-O-Si in SiO4 tetrahedra [15], [16].

3

Figure 4 and Figure 5 show the FTIR spectra of samples A and B with different hydration times and the concurrent changes in the spectra namely the shift towards lower wave numbers of band *(vi)* (450cm^{-1}) as hydration proceeds, indicating the formation of C-S-H structures like tobermorite by the in-plane bending of the Si-O bond [9], [11], [17]. This observation also suggests a more organized environment when compared to the anhydrous sample. In Figure 4 can also be seen the attenuation of the *(i)* band associated to structures like Wollastonite indicating a consumption of this phase as hydration proceeds, confirming the results obtained by XRD/Rietveld. Also, concerning sample A, a narrowing and intensification of the of band *(ii)* indicating a higher quantity of Q^2 units in the structure. In Figure 5, in addition to the observations made for Figure 4, the growth of the band approximately at 670cm^{-1} reinforces the evidences of the formation of C-S-H structures, as it has been attributed to de bending of the Si-O-Si in these structures [9], [17]. Finally, there is also a wide band between 1400-1500cm^{-1} associated with the asymmetric stretching of CO_3^{2-}, and two bands($\sim$1640 and 3540cm^{-1}) associated with the stretching vibrations of O-H in H_2O [9], [11]–[13], [16].
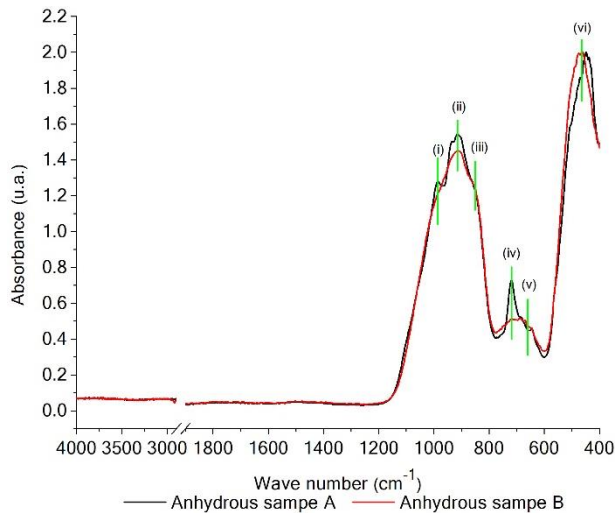

Figure 3 – FTIR-ATR spectrum of both A and B anhydrous samples.
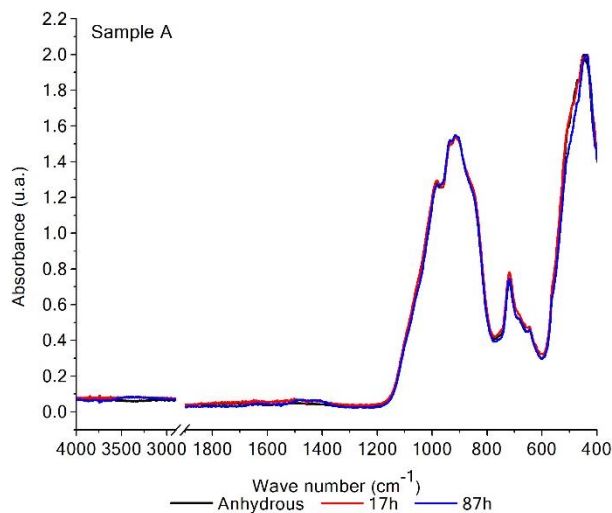

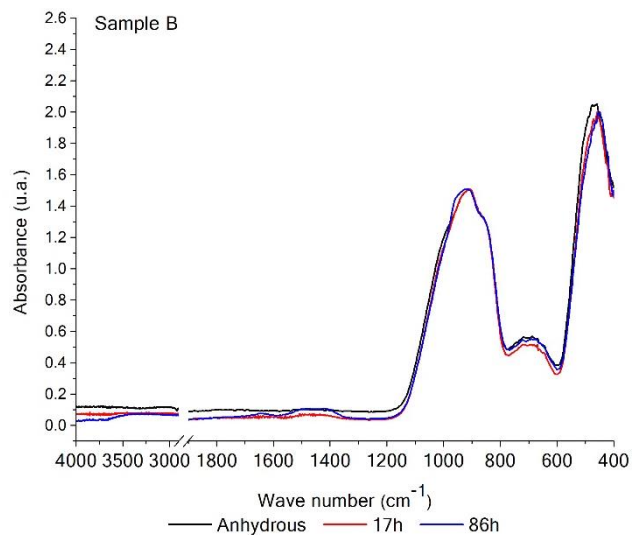**Figure 4 - FTIR-ATR spectrum for Sample A anhydrous, and with 17 and 87 hours of hydration.**

Figure 5 - FTIR-ATR spectrum for Sample B anhydrous, and with 17 and 86 hours of hydration.

3.1.4. SEM

Figure 6 and Figure 7 show both the anhydrous and hydrated samples A and B at two different magnifications. Figure 6 a) and Figure 7 a) show the surfaces of the anhydrous samples, at a magnification of 5000X, smooth and with almost no roughness indicating that the roughness seen in the images of the hydrated samples is a result of the hydration process. This characteristic is quite important because when in contact with water this allows for a higher contact promoting higher degree of hydration. The hydrated samples A and B have 71 and 91 days of hydration, respectively. In Figure 6 b) and Figure 7 b) hydration of the sample has occurred leading to the formation of a three-dimensional network of C-S-H lamellas replacing almost completely the smooth anhydrous surfaces. These lamellae form and grow at the expense of anhydrous particles. Their aspect bears a resemblance to the description of the C-S-H formed with a C/S<1.5 [18]–[21]. Despite the formation of these lamellae being evident in both types of samples, in Sample B these features appear to be in higher quantity and more homogenously spread throughout the sample. This leads to the conclusion that the degree of hydration in sample B is higher than in sample A. This could be related to the difference in hydration time but, at this stage of hydration the rates at which hydration products form are not enough to explain this difference.
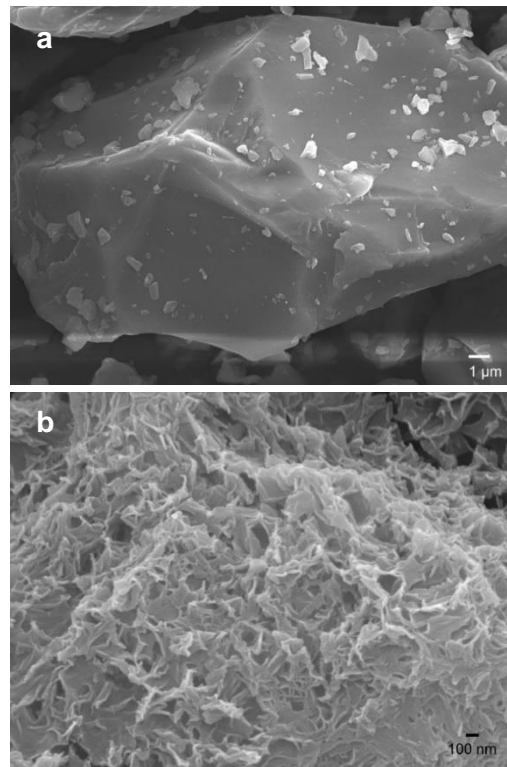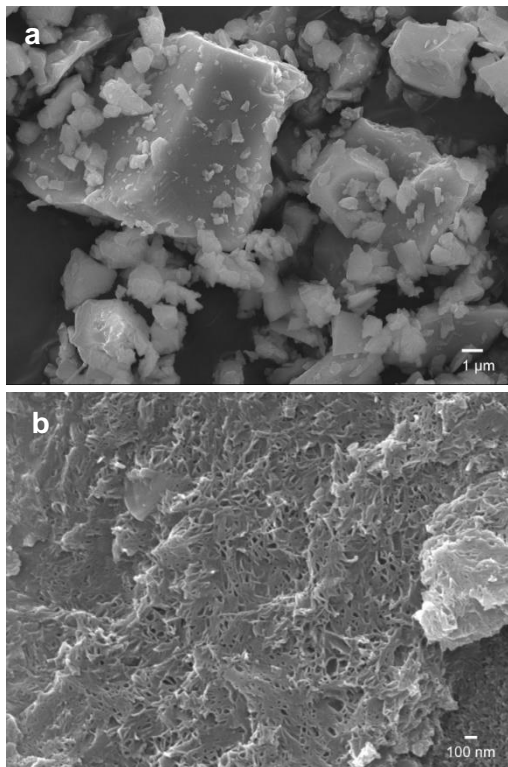
4

Figure 6 – SEM images of Sample A a) anhydrous at a magnification of 5000 X b) 71 days hydrated at a magnification of 30 000 X.

Figure 7 – SEM images of Sample B a) anhydrous at a magnification of 5000 X b) 71 days hydrated at a magnification of 30 000 X.
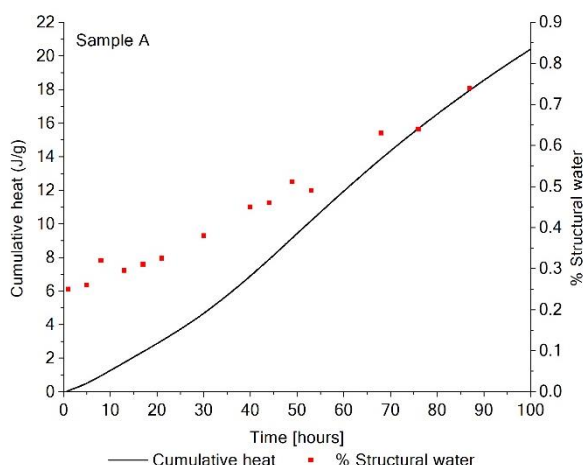

Figure 8 – Relationship between the cumulative heat curve and the percentage of structural water as a function of time for sample A.
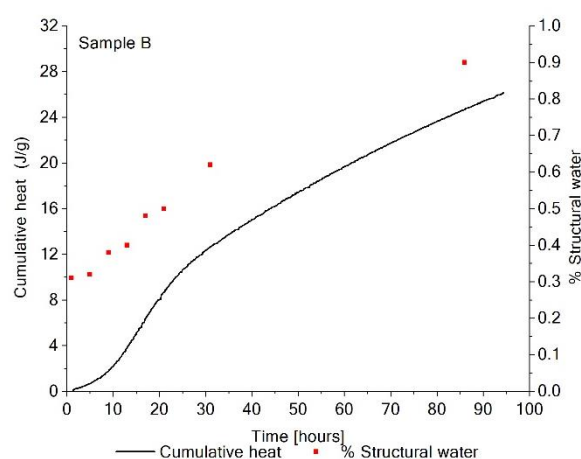

Figure 9 - Relationship between the cumulative heat curve and the percentage of structural water in function of time for Sample B.

3.1.5. Thermogravimetric analysis (TGA)

Figure 8 and Figure 9 show the TGA results and the cumulative heat curves plot against time for both samples A and B, respectively. In both cases the evolution of the structural water in the samples follows the heat released from the sample indicating that those two measurements are interconnected. Also, the fact that both samples follow this trend suggests that the mechanism by which they both hydrate is the same, diverging in the initial capacity of retaining water and in the hydration kinetics. Considering the results obtained by Santos [22] for samples equivalent to the samples A, FTIR and XRD results of those samples show equivalent behaviour when compared to samples A both when anhydrous and when hydrated allowing for a parallel to be made. The results obtained by Santos [22] for the RMN [29]Si MAS technique would therefore be expected to be very close to the ones that would be obtained if we

were to apply this technique to Sample A. In that sense, those results will be used in this is discussion as if they correspond to the samples studied here. Table 4 shows the results for the distribution of Q^n units for the deconvolution of RMN [29]Si MAS spectre of anhydrous and 28 days hydrated (with and without activator) samples alike the samples A studied here.

Looking to the results obtained from FTIR and comparing with the ones on Table 4, both show a predominance of Q^1 and Q^2 units in the samples although the results from RMN [29]Si MAS show also a percentage of 11.23% of Q^3 units that are difficult to identify by FTIR. This may happen because in the case of this type of units there is an overlap of signals in FTIR. Nevertheless, it can also be seen that in either case there is a reduction of the Q^0 and Q^1 units from amorphous material and a formation of Q^1 and Q^2 units of C-S-H. This strongly suggests a higher degree of polymerization with the evolution of hydration and a

5

tendency to form a more ordered structure with exclusively Q^2 units. There is also indication that the degree of instability in these amorphous hydraulic binders favours this rearrangement.

It is known that structures like rankinite and wollastonite do not react when hydrated, contrarily to structures like alite and belite, so comparing the characteristics of their structures, a hypothesis for why structures like wollastonite and rankinite do not hydrate was created. It may be assumed that they do not hydrate because their stable and ordered crystalline structure composed of Q^2 units when in contact with water and/or water and an activator cannot be sufficiently destabilized to allow for rearrangement and hydration of the sample. To try to prove this hypothesis a sample of almost fully crystalline wollastonite was produced and hydrated with the addition of an activator (Na_2SiO_3), and its hydration was followed by isothermal calorimetry. The results showed that no heat was released from the sample and no setting or hardening happened up to 28 days of hydration. This confirms the hypothesis that wollastonite has a stable enough structure to withstand hydration with water or with water and Na_2SiO_3 and not be destabilized by it. This result may also be assumed to occur when hydrating a rankinite sample in the same conditions.

Consequently, it can be concluded that the mechanism that allows for these amorphous hydraulic binders to hydrate is the rearrangement of the Q^n units in the anhydrous sample (Q^0, Q^1 and Q^3) triggered by the structure's metastable state. This rearrangement will lead to the formation of Q^2 hydrated units (amorphous C-S-H and tobermorite). This reaction can be enhanced by the addition of an activator like Na_2SiO_3 that will increase the pH of the solution promoting the dissolution of calcium ions and will also add to the mixture Q^0 units that will improve the reactivity, accelerating the hydration process. This mechanism is thought to happen in both samples A and B given that they have identical behaviours upon hydration.

Finally, it can be concluded that water cooling is the procedure that allows for the best mechanical response upon hydration and the one that produces the material with higher amorphous content.

Table 4 – Distribution of Q^n units obtained by deconvolution of RMN ^{29}Si MAS spectres for samples similar to sample A: anhydrous, not activated and activated with Na_2SiO_3 with 28 days of hydration [22].

Sample	Molar % of Si						
	$Q^0_{amorphous}$	Q^1_{C-S-H}	$Q^1_{amorphous}$	$Q^2_{Pseudowollastonite}$	$Q^2_{amorphous}$	Q^2_{C-S-H}	$Q^3_{amorphous}$
Anhydrous	8.98	---	29.23	12.51	38.04	---	11.23
Not activated	3.33	5.23	26.38	15.18	37.90	5.23	6.75
Na_2SiO_3	1.42	11.21	12.25	14.58	37.34	18.01	5.18

3.2. OPTIMIZATION OF HYDRATION CONDITIONS

All the samples produced in this study were water cooled. Seven types of samples were prepared initially only changing the W/C ratio, and in a second phase the W/C ratio was fixed and the particle sizes of the samples were changed. Table 5 the characteristics of each sample produced and the corresponding code.

Table 5 – Characteristics of samples production and each given code.

Sample	Particle size			W/C ratio		
	1 (180s)	2 (120s)	3 (45s)	0.325	0.375	0.425
A1_0.325	x			x		
A1_0.375	x				x	
A1_0.425	x					x
A2_0.375		x			x	
A3_0.325			x	x		
A3_0.375			x		x	
A1+3_0.375	x		x		x	

3.2.1. Specific surface

Blaine method was applied to the samples produced with different grinding times. Table 6 presents the values obtained with this method showing the surface areas for each sample and confirming that the samples have different particle sizes.

Table 6 – Specific surface area values for each particle size used.

	A1	A2	A3	A1+3
$S [cm^2 . g^{-1}]$	5135	4573	3242	4463

3.2.2. FTIR-ATR

Figure 10 and Figure 11 show the FTIR spectra obtained for all the samples tested in this study at three hydration times (7, 14 and 28 days of hydration). In both figures, there is a clear evolution of the samples over time towards a more ordered environment. All samples have six highlighted bands corresponding to the bands where the major changes occurred. Bands *(i)* and *(ii)* at around 3540 and 1640cm^{-1} are associated with stretching vibrations in O-H groups of H_2O, while the wide band *(iii)* between 1500-1400cm^{-1} has been associated with the asymmetric stretching of CO_3^{2-} [9], [11]–[13], [16]. It is possible to observe that with the progression of hydration the bands corresponding to the presence of water in the sample tend to have a higher intensity indicating a progressively higher amount of structural water. Continuing to lower wave numbers, two bands appear *(iv)* and *(v)* located in a region dominated by the stretching modes of non-bridging oxygens in Si-O for units Q^1 (900cm^{-1}) and Q^2 (950cm^{-1}) [9]–[13]. Upon hydration band *(iv)* gets attenuated while band *(v)* becomes more intense indicating a lower quantity of Q^1 units in the structure and a higher quantity of Q^2 units associated with the formation of C-S-H in the samples [13], [17]. This observation supports the rearranging mechanism of the units forming Q^2 units. Also, the band *(vii)* becomes more intense with hydration as it has been associated with the bending of the Si-O-Si in C-S-H structures like tobermorite [9], [17]. Band *(viii)* on the other hand does not get more intense but gets sharper as it is associated with the in-plane bending of Si-O bond in C-S-H structures like tobermorite [9], [11], [17]. The shift of these two bands

towards lower wavenumbers suggest a more organized environment.

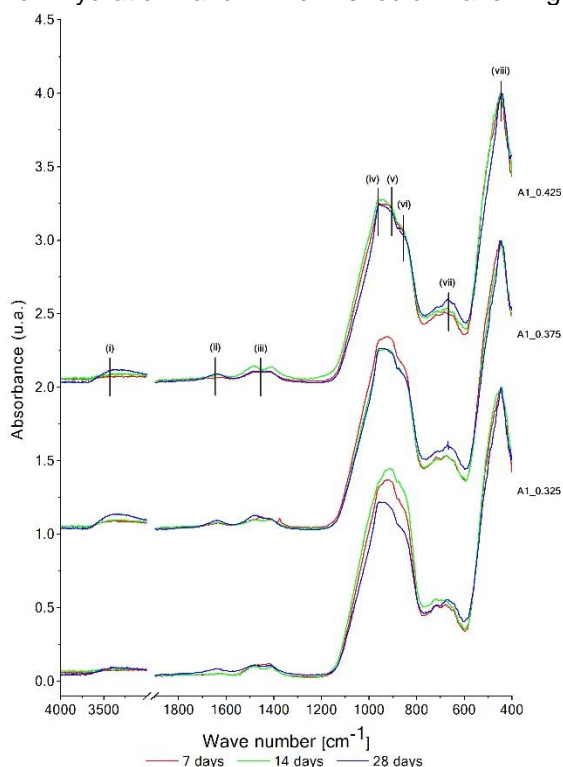These various changes in the samples' spectra allows to identify which of the samples appear to have a higher degree of hydration and which should have higher compressive strengths at each hydration time. The samples that show a more advanced hydration when only considering FITR spectra are A1_0.425, A1_0.375 and A2_0.375.
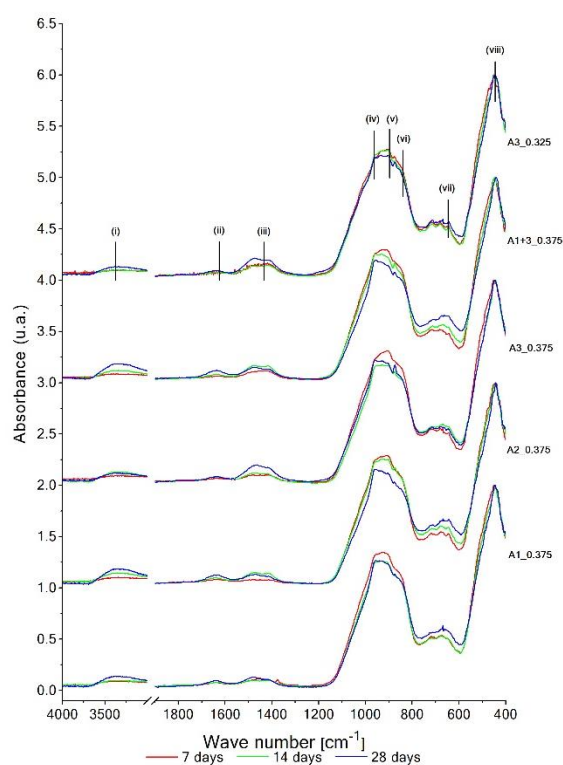

Figure 10 - FTIR-ATR spectrums for samples A1_0.425, A1_0.375, A1_0.325 with 7, 14 and 28 days of hydration.

Figure 11 - FTIR-ATR spectrums for samples A1_0.375, A2_0.375, A2_0.375 and A1+3_0.375 with 7, 14 and 28 days of hydration.

3.2.3. XRD/Rietveld

Table 7 and Table 8 show the phase percentages obtained by Rietveld fitting for all the samples produced in this study at 4, 7, 14 and 28 days of hydration.

An increase in the amount of crystalline C-S-H produced can be seen as hydration progresses for every sample, being sample A1_0.375 the one that presents the higher value. Regarding wollastonite, there is an apparent tendency for its consumption that was not visible in the Rietveld fitting of sample B in the previous chapter. This difference probably has to do with the short hydration times at which sample B was analysed. This consumption might have to do with the carbonation of wollastonite with the contact with CO_2 [6], [7].

3.2.4. SEM/EDS

Figure 12 shows SEM images of the fractured surfaces of the samples with different particle sizes hydrated with the same W/C ratio at 20 days of hydration. There are clear differences in degree of hydration from sample to sample and because the hydration time for all the samples is the same a direct comparison can be made. The sample from Figure 12 a) is clearly the one with a higher degree of hydration and the one where the three-dimensional network of lamellas is more developed. As also suggested above, these lamellas form and grow at the expense of anhydrous particles (Figure 7 a)) which have a smooth surface and the network formed has an identical appearance to the one reported to form in C-S-H structures with a C/S<1.5 [18]–[21]. From the observation of the other images in Figure 12, it can be seen that the degree of hydration of the samples has the following trend A3_0.375<A1+3_0.375<A2_0.375<A1_0.375.

3.2.5. Compressive strength testing

Figure 13 and Figure 14 show the results obtained for the compressive strength development of the various samples produced in this study. The sample showing higher mechanical performance development is A1_0.325, which is within the expected, since this is the sample that minimizes the effect of water porosity contribution to the strength of the pastes. Excess water contributes not only for an increase in porosity but also represents a barrier to the formation of an interconnected network of hydration products. From the moment enough water to hydrate all the particles is given to the mixture, the excess water will only make the sample take more time to set and harden and make it work as an oversaturated system. This also separates the particles so that, even though the sample forms hydration products with strength themselves, it cannot gain the expected strength because those products are not close to each other. However, all excess water added to the samples will improve workability of the pastes. Comparing both figures, it can be seen that all samples follow almost the same progression trend, the main difference between them being the initial capacity to develop compressive strength.

7

Table 7 – Rietveld analysis of samples with same particle size but hydrated with different W/C ratios, at 4, 7, 14 and 28 days of hydration.

Sample	Age (days)	Phases (wt.%)		
		Amorphous	Wollastonite	Tobermorite 9Å
A1	Anhydrous	98.0	2.0	-
A1_0.325	4	96.6	1.4	2.0
A1_0.325	7	96.7	1.2	2.1
A1_0.325	14	96.9	1.0	2.1
A1_0.325	28	96.0	1.1	2.9
A1_0.375	4	96.8	1.4	1.8
A1_0.375	7	96.6	1.2	2.3
A1_0.375	14	95.0	1.4	3.6
A1_0.375	28	95.0	1.2	3.7
A1_0.425	4	97.1	1.5	1.3
A1_0.425	7	96.7	1.3	2.0
A1_0.425	14	96.2	1.2	2.7
A1_0.425	28	95.4	1.1	3.5

Table 8 - Rietveld analysis of samples with same W/C ratios and different particle sizes, at 4, 7, 14 and 28 days of hydration. Is also represented the sample A3_0.325.

| Sample	Age (days)	Phases (wt.%)		
		Amorphous	Wollastonite	Tobermorite 9Å
A1/A2/A3	Anhydrous	98.0	2.0	-
A3_0.325	7	95.7	3.1	1.2
A3_0.325	14	94.8	2.8	2.4
A3_0.325	28	93.5	2.7	2.8
A1_0.375	4	96.8	1.4	1.8
A1_0.375	7	96.6	1.2	2.3
A1_0.375	14	95.0	1.4	3.6
A1_0.375	28	95.0	1.2	3.7
A2_0.375	4	95.7	2.5	1.9
A2_0.375	7	95.6	2.2	2.2
A2_0.375	14	95.6	2.1	2.3
A2_0.375	28	95.5	2.0	2.5
A3_0.375	4	96.2	2.3	1.5
A3_0.375	7	96.0	2.3	1.7
A3_0.375	14	95.4	2.1	2.5
A3_0.375	28	94.8	2.4	2.8
A1+3_0.375	4	96.3	2.0	1.7
A1+3_0.375	7	96.0	2.0	2.0
A1+3_0.375	14	95.6	1.9	2.5
A1+3_0.375	28	95.5	1.9	2.6
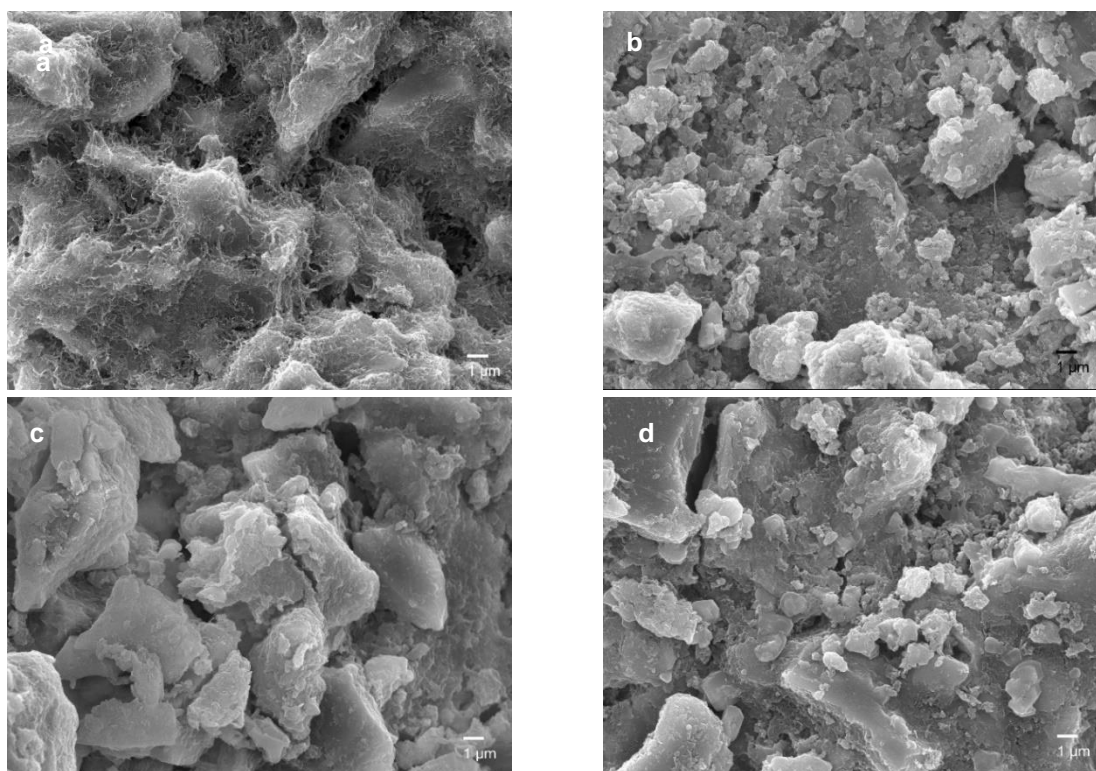
Figure 12 – SEM images with a 5000X magnification of the samples: a) A1_0.375; b) A2_0.375; c) A3_0.375; e d) A1+3_0.375.
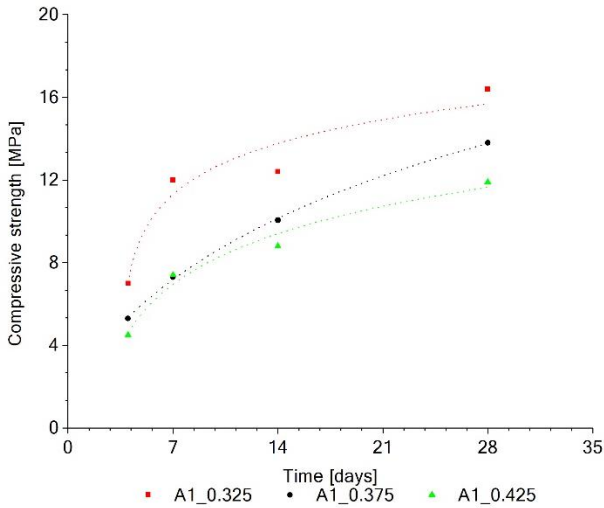
Figure 13 – Compressive strength development of samples with same granulometric distribution and different W/C ratios.
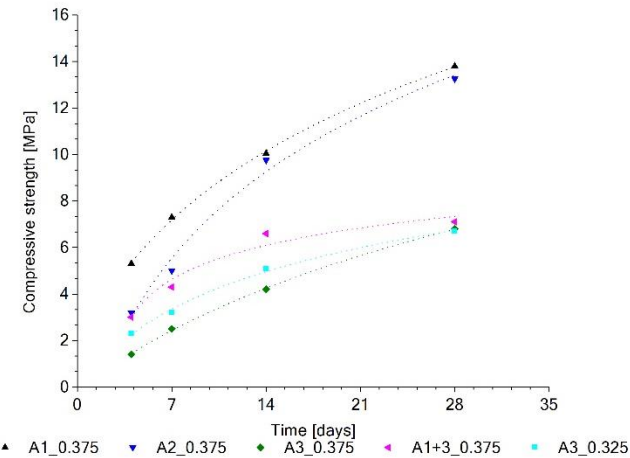

Figure 14 – Compressive strength development of samples with same W/C ration and different granulometric distributions. Is also represented the sample A3_0.325.

Figure 14 depicts the effect of varying the surface area available for hydration while maintaining the W/C ratio. With the decrease in surface area, the water needed for complete hydration of the particles decreases, making for the samples where too much water is given to the paste to have lower compressive strengths. This can be observed in Figure 14 where the sample with highest surface area (A1_0.375) presents the highest compressive strength and the one with the lowest surface area (A3_0.375) shows the lowest results, for the same W/C ratio. Sample A1+3_0.375 is a combination of two types of particles with different surface areas, therefore having a mixed reactivity, being that it showed a good reactivity in the beginning of hydration due to the fraction of smaller particles in the sample but the rate of hydration was not maintained as hydration progressed because the other fraction of particles were much larger slowing down the rate of hydration. At 28 days of hydration this sample showed a similar compressive strength as sample A3_0.375, allowing for the conclusion that the mixing of two types of particles does not offer advantages when compared to the other samples tested. Considering the results obtained for sample A3_0.375 it was thought that there was some margin for progression and so sample A3_0.325 was produced. The results for this sample showed some progression when compared to the same

particle sizes but with a higher W/C ratio both in compressive strength and in structural water gaining.

3.2.6. Viscosity testing

Viscosity testing was performed on every sample tested in this study in order to evaluate workability. Because workability cannot be evaluated by viscosity testing alone, the results coming from this test have to be evaluated as a comparison to the viscosity of the CEM II cement used as reference and a certain degree of subjectivity must also be taken into account in respect to "easiness to spread" the pastes produced is concerned.

Table 9 depicts the values of viscosity obtained for each sample produced. The sample that has the closest value to the one of CEM II is A1_0.375. Notwithstanding this, sample A2_0.375 despite having a much lower value than CEM II is a sample that has a workability as good as the one of A1_0.375. Although sample A1_0.325 also has a similar viscosity value to the one of CEM II, the fact that it has a higher viscosity means that it probably is less workable.

Table 9 – Viscosity values for each sample produced.

Sample	Viscosity [Pa.s]
CEM II	3
A1_0.325	--
A1_0.375	2.5
A1_0.425	0.7
A2_0.375	1.2
A3_0.325	0.8
A3_0.375	0.125
A1+3_0.375	0.9

3.2.7. Thermogravimetric analysis (TGA)

Figure 15 and Figure 16 depict the relationship between compressive strength and bound water as hydration proceeds for every sample produced in this study. The applied changes in W/C ratio and in particle size both lead to important alterations in hydration kinetics and mechanical testing. Despite the differences between them the development tendency of every sample is the same as all the tendency curves are almost parallel to each other.

In Figure 15 the main difference between samples is the initial capacity of the samples to gain compressive strength with barely the same percentage of bound water. This might be an indication that samples A1_0.375 and A1_0.425 both have hydration products that are further apart from each other limiting the compressive strength gain. On the other hand, on Figure 16 the situation is not the same. Here, as particle size is changed, there are significant changes both in bound water and in compressive strength. Despite this shift, the rate at which the samples evolve is the same, meaning that the difference is on the initial capacity of gaining bound water and compressive strength. The most promising samples are A1_0.325, A1_0.375 e A2_0.375.
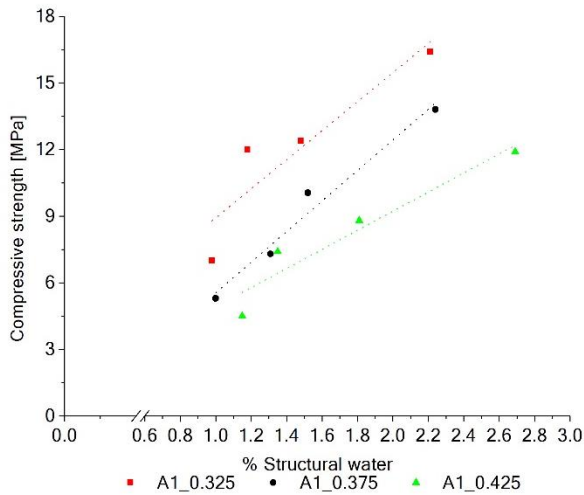
Figure 15 - Relationship between water structural water in each sample and compressive strength for the samples with the same granulometric distribution and with different W/C ratios.
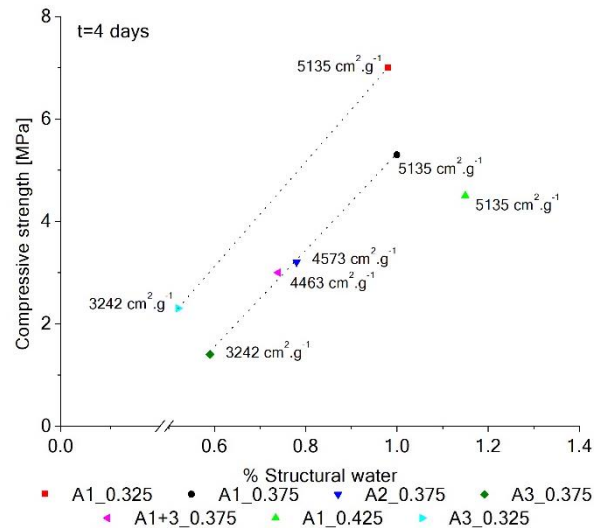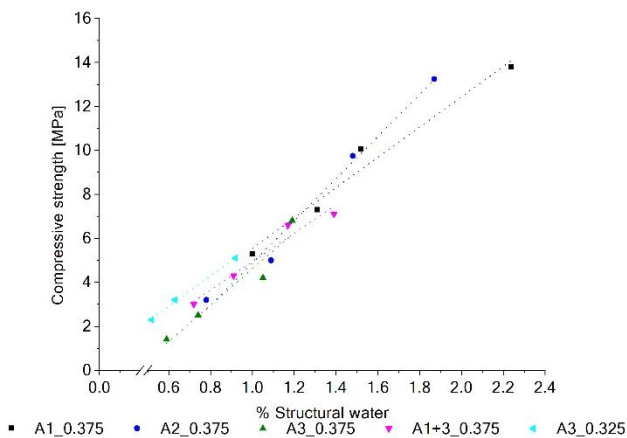

Figure 16 - Relationship between water structural water in each sample and compressive strength for the samples with the same W/C ratio and different granulometric distributions. Is also represented the sample A3_0.325.

Figure 17 shows the relationship between compressive strength and percentage of bound water in each sample, after four days of hydration. As surface area of the samples increases, there is a progressive growth in the compressive strength as well as in the percentage of bound water for a given W/C ratio. With this relationship, it could be assumed that if we were to hydrate a sample with a surface area between 4573 and 5135 $cm^2.g^{-1}$ and a W/C ratio of 0.375 the compressive strength/percentage of bound water ratio could be determined. This relationship is clear for the W/C ratio of 0.375, allowing for the supposition that for the other two W/C ratios the same kind of relationship could be found.

Figure 17 - Relationship between water structural water in each sample and compressive strength for every sample, after four days of hydration.

4. CONCLUSIONS

Two amorphous hydraulic binders were synthesized with different cooling conditions: air- and water-cooling. In both cases a material constituted by more than 90% of an amorphous phase was obtained.

Through the combination of various techniques, it could be concluded that the mechanism by which the present amorphous hydraulic binders hydrate is through the rearrangement of the Q^n units present in the anhydrous samples (Q^0, Q^1 and Q^3) induced by their metastability. This rearrangement leads to the formation of Q^2 hydrated units (amorphous C-S-H and tobermorite). Because samples A and B have identical behaviour upon hydration, it can be said that the mechanism by which they both hydrate is the same. Also through this study it can be concluded that water cooling is the procedure that allows for the best mechanical performance upon hydration and the one that produces the material with higher amorphous (~98 wt. %) content and higher instability.

From the optimization of hydration conditions study, and considering the result of compressive, TGA and viscosity testing, the samples that produce the best combination of results both in workability and mechanical strength are A1_0.375 and A2_0.375. The choosing between these two samples requires further study on their long-term evolution. However, sample A2_0.375 is the one that shows the most promising results being the one that is chosen by the authors as the most suitable one.

5. BIBLIOGRAPHY

[1]   'Global Cement Database on CO_2 and Energy Information'. [Online]. Available: http://www.wbcsdcement.org/index.php/key-issues/climate-protection/gnr-database. [Accessed: 07-Sep-2017].

[2]   'Development of State of the Art-Techniques in Cement Manufacturing : Trying to Look Ahead', 2017.

[3]   R. L. Santos, R. B. Horta, J. Pereira, T. G. Nunes, P. Rocha, J. N. C. Lopes, and R. Cola??o, 'Novel high-resistance clinkers with 1.10 < CaO/SiO2 < 1.25: Production route and preliminary hydration characterization', *Cem. Concr. Res.*, vol. 85, pp. 39–47, 2016.

[4]   H. F. W. Taylor, *Cement chemistry*, 2nd ed. Thomas Telford Publishing, 1997.

[5]   J. W. Bullard, H. M. Jennings, R. A. Livingston, A. Nonat, G. W. Scherer, J. S. Schweitzer, K. L. Scrivener, and J. J. Thomas, 'Mechanisms of cement hydration', *Cem. Concr. Res.*, vol. 41, no. 12, pp. 1208–1223, 2011.

[6]   W. J. J. Huijgen, G. J. Witkamp, and R. N. J. Comans, 'Mechanisms of aqueous wollastonite carbonation as a possible CO2 sequestration process', *Chem. Eng. Sci.*, vol. 61, no. 13, pp. 4242–4251, 2006.

[7]   W. Ashraf and J. Olek, 'Carbonation behavior of hydraulic and non-hydraulic calcium silicates: potential of utilizing low-lime calcium silicates in cement-based materials', *J. Mater. Sci.*, vol. 51, no. 13, pp. 6173–6191, 2016.

[8]   J. Bensted and P. Barnes, Eds., *Structure and Performande of Cements*, 2nd ed. Spon Press, 2002.

[9]   P. Yu, R. J. Kirkpatrick, B. Poe, P. F. McMillan, and X. Cong, 'Structure of Calcium Silicate Hydrate (C-S-H): Near-, Mid-, and Far-Infrared Spectroscopy', *J. Am. Ceram. Soc.*, vol. 82, no. 3, pp. 742–748, 1999.

[10]   M. Handke, M. Sitarz, and W. Mozgawa, 'Model of silicooxygen ring vibrations', *J. Mol. Struct.*, vol. 450, no. 1–3, pp. 229–238, 1998.

[11]   I. García-Lodeiro, A. Fernández-Jiménez, M. T. Blanco, and A. Palomo, 'FTIR study of the sol-gel synthesis of cementitious gels: C-S-H and N-A-S-H', *J. Sol-Gel Sci. Technol.*, vol. 45, no. 1, pp. 63–72, 2008.

[12]   C. Paluszkiewicz, M. Blazewicz, J. Podporska, and T. Gumuła, 'Nucleation of hydroxyapatite layer on wollastonite material surface: FTIR studies', *Vib. Spectrosc.*, vol. 48, no. 2, pp. 263–268, 2008.

[13]   I. Lecomte, C. Henrist, M. Liégeois, F. Maseri, A. Rulmont, and R. Cloots, '(Micro)-structural comparison between geopolymers, alkali-activated slag cement and Portland cement', *J. Eur. Ceram. Soc.*, vol. 26, no. 16, pp. 3789–3797, 2006.

[14]   D. De Sousa Meneses, M. Malki, and P. Echegut, 'Optical and structural properties of calcium silicate glasses', *J. Non. Cryst. Solids*, vol. 352, no. 51, pp. 5301–5308, 2006.

[15]   S. A. MacDonald, C. R. Schardt, D. J. Masiello, and J. H. Simmons, 'Dispersion analysis of FTIR reflection measurements in silicate glasses', *J. Non. Cryst. Solids*, vol. 275, pp. 72–82, 2000.

[16]   R. D. Husung and R. H. Doremus, 'The infrared transmission spectra of four silicate glasses before and after exposure to water', *J. Mater. Res.*, vol. 5, no. 10, pp. 2209–2217, 1990.

[17]   P. A. Bhat and N. C. Debnath, 'Theoretical and experimental study of structures and properties of cement paste: The nanostructural aspects of CSH', *J. Phys. Chem. Solids*, vol. 72, no. 8, pp. 920–933, 2011.

[18]   R. Ylmén, U. Jäglid, B.-M. Steenari, and I. Panas, 'Early hydration and setting of Portland cement monitored by IR , SEM and Vicat techniques', *Cem. Concr. Res.*, vol. 39, no. 5, pp. 433–439, 2009.

[19]   P. Hewlett, *Lea's Chemistry of Cement and Concrete*, 4th ed., vol. 58, no. 10. Elsevier Science & Technology Books, 2004.

[20]   R. Vigil De La Villa, R. Fernández, O. Rodríguez, R. García, E. Villar-Cociña, and M. Frías, 'Evolution of the pozzolanic activity of a thermally treated zeolite', *J. Mater. Sci.*, vol. 48, no. 8, pp. 3213–3224, 2013.

[21]   R. Vigil de la Villa, R. Fernández, R. García, E. Villar-Cociña, and M. Frías, 'Pozzolanic activity and alkaline reactivity of a mordenite-rich tuff', *Microporous Mesoporous Mater.*, vol. 126, no. 1–2, pp. 125–132, 2009.

[22]   R. Lino Santos, 'New Hydraulic Binders with Low Calcium Content', Universidade de Lisboa, 2016.